4 TRAPPING AN IRON(VI) WATER SPLITTING INTERMEDIATE IN NONAQUEOUS MEDIA

4.1 Summary

The sustainable and economical conversion of solar energy into storable, transportable fuels by solar-driven water splitting is a grand challenge of 21st century chemistry. The mechanisms by which heterogeneous materials perform the anodic half-reaction, water oxidation, are not well understood. In this chapter, we describe *in-situ* spectroscopic measurements in nonaqueous media designed to trap an exceptionally strong oxidant generated electrochemically from an iron-containing nickel layered double hydroxide ([NiFe]-LDH) material. Anodic polarization of this material in acetonitrile produces prominent infrared absorption features (840 and 856 cm^{-1}) that are quenched by the addition of water. These vibrational spectroscopic signatures along with a potential-dependent extremely narrow luminescence peak at 1633 nm indicate that the reactive intermediate is a *cis*-dioxo-iron(VI) species. An absorption in the Mössbauer spectrum of the material, which disappears upon exposure to alkaline acetonitrile, is consistent with population of a high-valent iron-oxo species. Importantly, chemical trapping experiments reveal that addition of H_2O to the polarized electrochemical cell produces hydrogen peroxide; and addition of HO^- generates oxygen. Re-polarization of the electrode restores the iron(VI) spectroscopic signatures, confirming that the high-valent oxo complex is active in the electrocatalytic water oxidation cycle. Our work demonstrates that *in-situ* spectroscopy in nonaqueous media offers a powerful new approach to the study of aqueous redox mechanisms.

4.2. Results

Nickel-iron layered double hydroxide ([NiFe]-LDH) nanoparticles are highly active catalysts for water oxidation at pH 14 (Figure 4.1)[1,2]. These nanocatalysts, which were synthesized by pulsed laser ablation in water[3], operate at low overpotentials for oxygen evolution on flat glassy carbon electrodes. Precisely because they are such active materials, steady-state concentrations of catalytic species are necessarily low under turnover conditions; indeed, initial experiments on [NiFe]-LDH resulted in conflicting reports on the identity of the catalytically relevant sites[4-7]. Consequently, there is little consensus about the operative mechanism for these (and other) water oxidation catalysts[8].

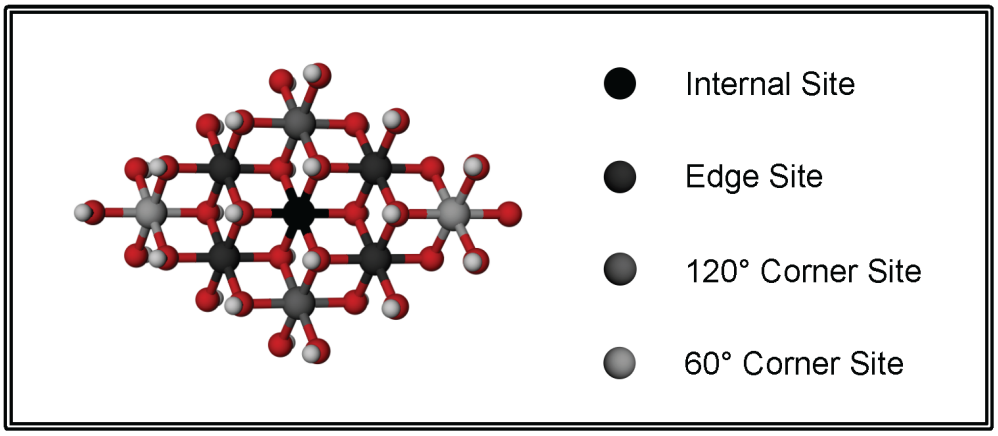

Figure 4.1. Structure of [NiFe]-LDH. In the [NiFe]-LDH material, a sheet of $Ni(OH)_6$ edge-shared octahedra contains a small amount (~20%) of iron substituting at nickel sites[9]. Different types of peripheral sites are indicated.

We have developed an alternative approach to examine reactive intermediates of highly active water-oxidation catalysts. Strasser, Dau, and coworkers suggested that the failure to observe oxidized metals in *operando* measurements on highly active [NiFe]-LDH electrodes is likely a consequence of oxygen evolution outpacing metal oxidation[7]. Under these circumstances, the steady state concentration of oxidized catalyst will be extremely

low. By using nonaqueous electrolytes (acetonitrile, nitromethane) in which the concentration of substrate (H_2O, HO^-) is reduced dramatically, the oxygen evolution rate is slowed sufficiently to permit formation of significant concentrations of reactive intermediates. Owing to the protracted reactive intermediate lifetime, we could use *in-situ* IR, UV-vis, Raman, luminescence, and Mössbauer spectroelectrochemistry to characterize a high-valent intermediate that subsequently reacted with H_2O to produce H_2O_2 and with HO^- to produce O_2. The results of our study suggest that a *cis*-dioxo-Fe(VI) species likely is an active intermediate in [NiFe]-LDH catalyzed water oxidation.

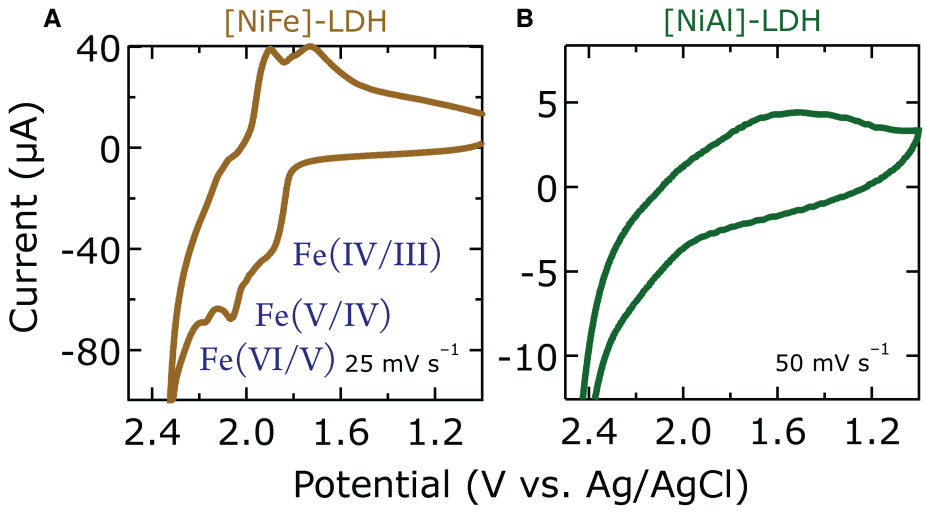

Figure 4.2. Cyclic voltammograms of [NiFe]-LDH (**A**) and [NiAl]-LDH (**B**) on glassy carbon in dry acetonitrile. $E°$(ferricenium/ferrocene) (Fc^+/Fc) was measured to be 410 mV under virtually identical conditions.

4.2.1. Electrochemistry

Under inert conditions (acetonitrile or nitromethane with 0.1 *M* [TBA]PF_6 (TBA = tetra-*n*-butylammonium) as the supporting electrolyte), cyclic voltammetry of [NiFe]-LDH films cast onto glassy carbon surfaces revealed three chemically reversible oxidations that were

absent in the iron-free analogue, [NiAl]-LDH (Figure 4.2). Because iron substitutes into the nickel-hydroxide lattice as Fe(III), we assign these oxidations to the sequential formation of Fe(IV), Fe(V), and Fe(VI), with smaller currents for each successive anodic process[10]. By reversing scans after each successive oxidation event and observing a coupled reduction, we concluded that the events were quasi-reversible on the electrochemical timescale (Figure 4.3). Closely spaced redox couples are not uncommon for proton-coupled electron transfer steps of molecular species; for example, $[Ru(II)(bpy)_2(OH_2)_2]^{2+}$ can achieve oxidation states II/III/IV/V/VI over a potential range of 0.6 V[11]. Assuming a formula of $Ni_{0.78}Fe_{0.22}(OH)_2(NO_3)_{0.22}$, we estimated from coulometry that ~0.002% of the iron sites are electrochemically active to make Fe(IV). Approximately half as many sites (0.001%) are active at the Fe(V/IV) couple, while only 0.0002% of the sites proceed to Fe(VI). The decrease in the number of electrochemically active sites at the higher potential couples is consistent with the limited number of atoms at edge and corner sites in ca. 10 nm nanosheets, suggesting that high-valent species are only formed at the perimeters of the particles.

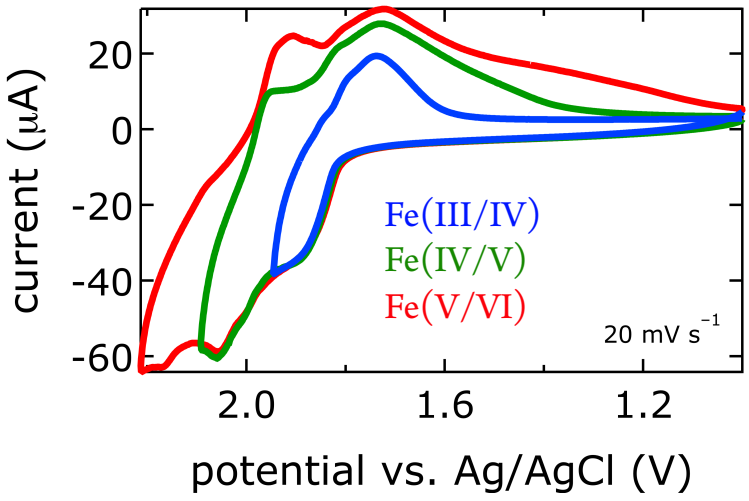

Figure 4.3. Cyclic voltammetry of [NiFe]-LDH in 0.1 M tetrabutylammonium hexafluorophosphate ([TBA]PF_6) in acetonitrile. The scans were reversed after each oxidative event, showing that each was coupled to a corresponding reduction. Scan rate was 20 mV/s.

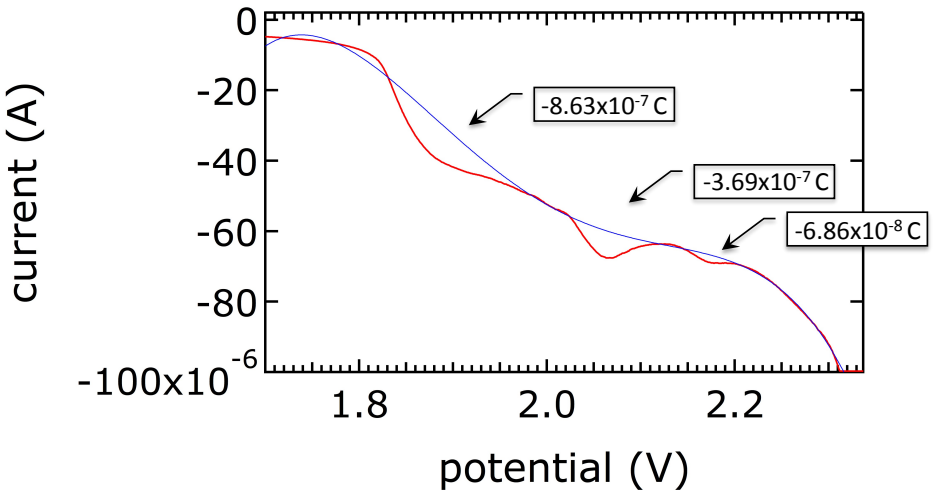

Figure 4.4. Cyclic voltammetry of [NiFe]-LDH in 0.1 M tetrabutylammonium hexafluorophosphate ([TBA]PF_6) in acetonitrile with baseline subtraction and charge passed integrated for the 3 iron-based features. Reference electrode: Ag/AgCl.

Table 4-1: Calculation of activity of iron in [NiFe]-LDH sample, based on coulometry of cyclic voltammetry.

	Charge Passed	Active Moles	% active
1st oxidation	-8.63×10^{-7}	8.94×10^{-12}	0.00237
2nd oxidation	-3.69×10^{-7}	3.82×10^{-12}	0.00101
3rd oxidation	-6.86×10^{-8}	7.11×10^{-13}	0.000188

4.2.2. Vibrational Spectroscopy

To probe the high-valent iron species, we monitored changes in the vibrational and electronic spectra of [FeNi]-LDH *via* controlled-potential spectroelectrochemistry[12]. The infrared difference spectrum recorded during bulk oxidation of [NiFe]-LDH in acetonitrile[13] exhibits prominent features at 840 and 856 cm^{-1}, with a small shoulder at 877 cm^{-1} (Figure 4.5**A**). Interestingly, the shoulder—whose intensity varied from one experiment to the next—appeared only after an induction period at a rate different from

that of the other two bands (Figure 4.5**C**). Although this oxidized intermediate was thermally stable in dry solvents, introducing "wet" electrolyte (5% water in 0.1 M [TBA]PF_6/acetonitrile) into the IR cell rapidly bleached the three main absorbances, suggesting that they correspond to an active intermediate in the water-oxidation pathway (Figure 4.5**B**)[14].

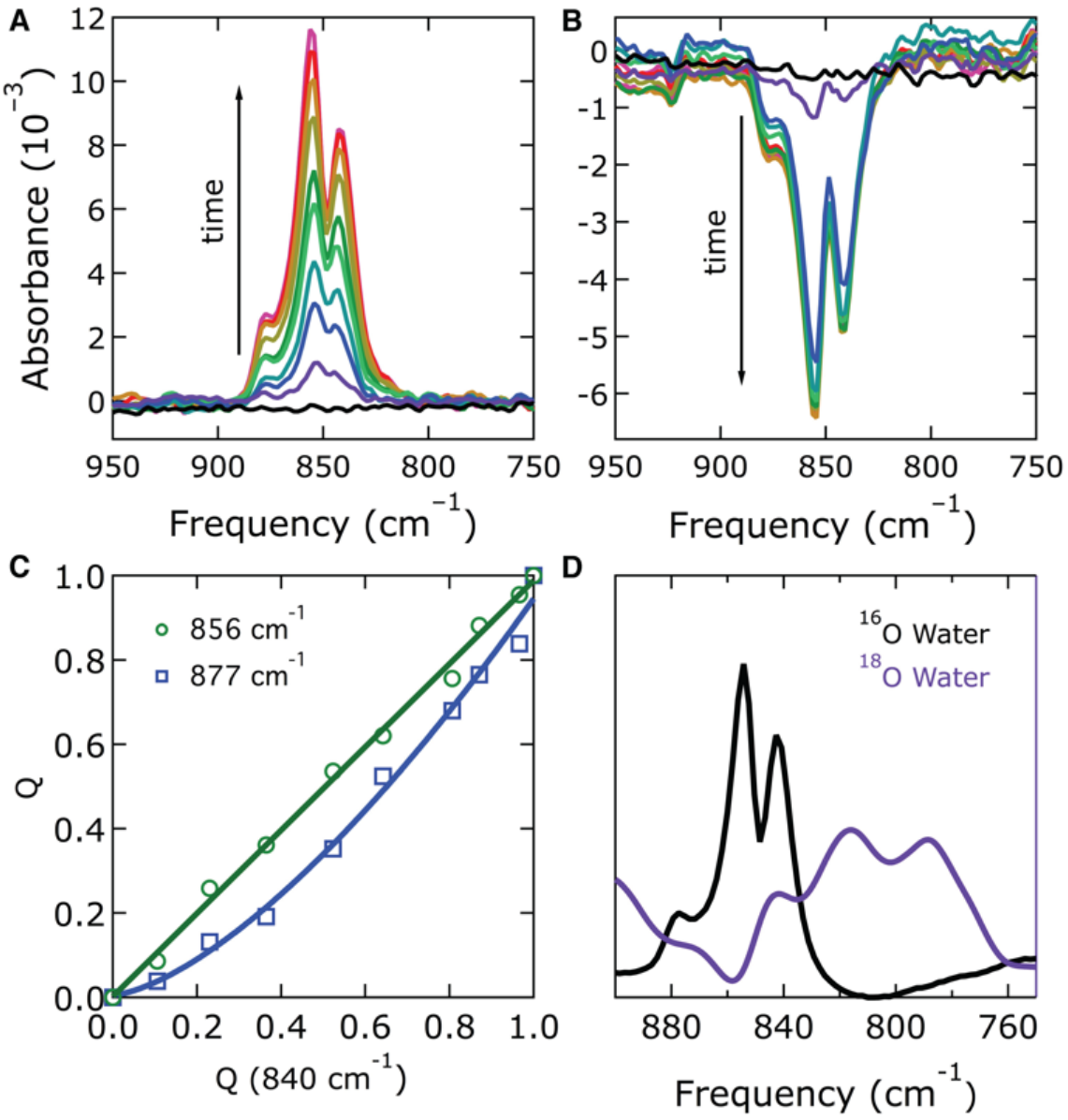

Figure 4.5. (**A**) Three-band signal growing in upon bulk oxidation in acetonitrile (2.3 V vs. Pt), 0.1 M [TBA]PF_6, on GC working electrode, Pt counter electrode, 30 sec. between spectra; (**B**) bleach of three-band signal upon injection of water, 30 sec. between spectra; (**C**) fractions of the final Lorentzian peak areas (Q) of the 856 and 877 cm^{-1} bands plotted versus the Q for the 840 cm^{-1} band; solid lines are fits to linear (green) and polynominal ($c_1 + c_2x^{c3}$) (blue) functions to emphasize the different trends; (**D**) exhaustive electrolysis isotope exchange in $H_2{}^{18}O$ followed by *in situ* infrared analysis.

The 840 and 856 cm^{-1} features in the spectrum are attributable to high-valent iron-oxo species. We considered the possible formation of both a mono-oxo Fe(IV)=O center[15] as well as a more highly oxidized *cis*-dioxo-Fe(VI) species—the latter by analogy to the tetraoxoferrate(VI) anion (FeO_4^{2-}). Because a mono-oxo Fe(IV)=O center would exhibit just a *single* Fe-O stretch, we assign the 840- and 856-cm^{-1} peaks to the antisymmetric and symmetric stretches of a *cis*-dioxo-Fe(VI) fragment. The symmetric and antisymmetric stretches of monomeric dioxo species are generally split by 10-30 cm^{-1}.[16-19] Using FeO_4^{2-} as a model for the putative dioxo-Fe(VI) species, DFT calculations predict considerable intensity for the Fe-O stretches in the infrared spectrum. Features corresponding to bending modes (<400 cm^{-1}) should also appear in the vibrational spectra (Figure 4.6). Subsequent *in-situ* Raman spectroelectrochemical oxidation of drop-cast [FeNi]-LDH films under virtually identical conditions revealed these bends at ~400 cm^{-1} (Figure 4.7).

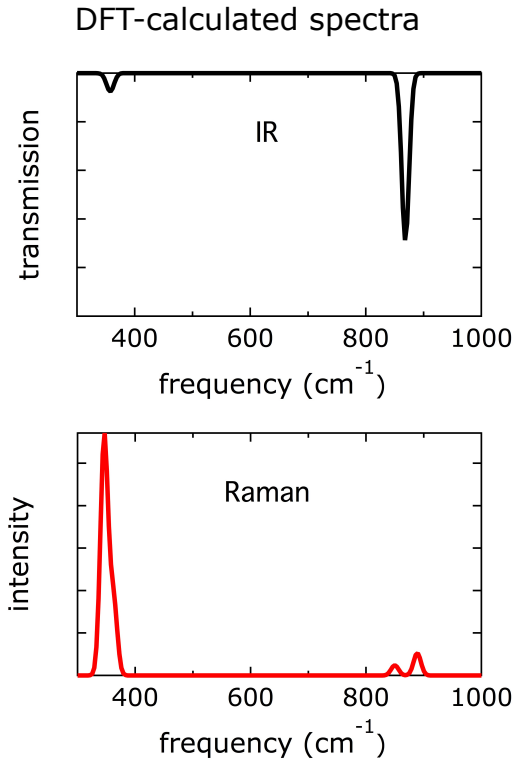

Figure 4.6. (Top) Calculated infrared spectrum for ferrate; (bottom) calculated Raman spectrum for ferrate.

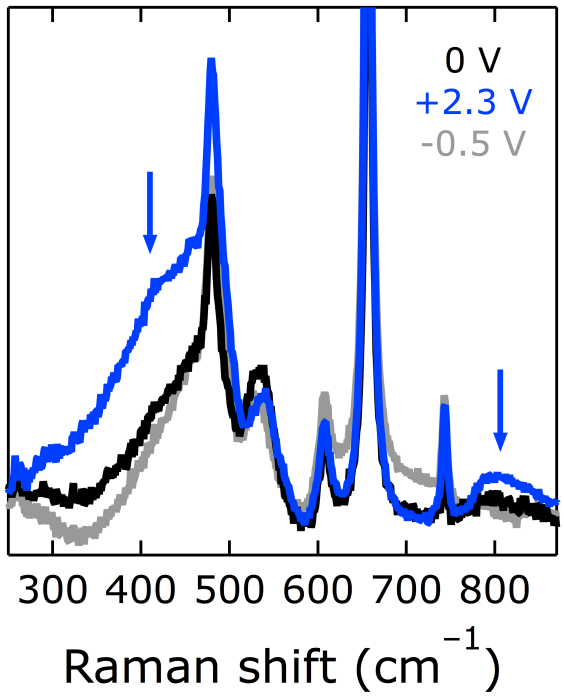

Figure 4.7. Raman spectroelectrochemistry experiment in nitromethane. Signal observed in the bending region (~400 cm^{-1}) upon polarization of the electrode at 2.3 V vs. Pt (blue). The signal is diminished upon cycling to -0.5 V vs. Pt (gray). Nitromethane, 0.1 M [TBA]PF_6, on GC working electrode, Pt counter electrode, and Pt reference electrode. The excitation wavelength was 514.3 nm.

Notably, based on its stretching frequency, we initially attributed the 875 cm^{-1} shoulder to free Fe(VI) in the form of soluble FeO_4^{2-}, which would be leached out of the material at low pH[20]. This was consistent with our observation that a purple substance sometimes appeared in the electrolyte solution after anodic polarization (Figure 4.8). Boettcher et al. previously reported that $Co_{1-x}Fe_x(OOH)$ films with $1 > x > 0.5$ slowly dissolve under water oxidation conditions[21]. It was later suggested that the dissolved species could be tetraoxoferrate(VI)[22]. Our inability to "wash out" the high-energy shoulder, however, indicated that it was due to a surface-bound moiety.

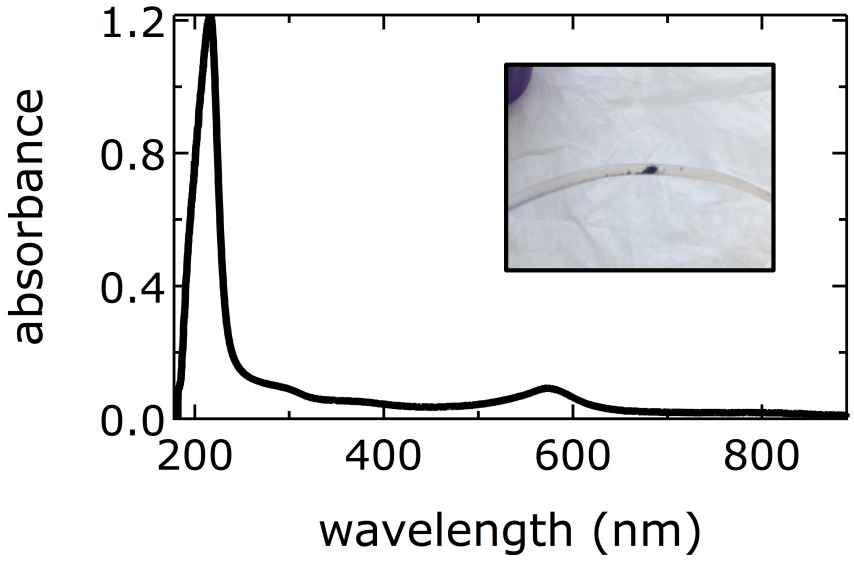

Figure 4.8. UV-visible spectrum of small volume electrolysis electrolyte following 10 minutes of anodic polarization; (Inset) typical purple substance that leaches out during spectroelectrochemistry experiments.

4.2.3. Isotope Labeling Studies

To shed additional light on these highly oxidized species, we carried out several experiments using isotopically labeled (^{18}O) water. Reproducing the 856 and 840 cm^{-1} features in the IR spectrum, we quenched the material with $H_2{}^{18}O$ water. After flushing the spectroelectrochemistry cell with 0.1 M $[TBA]PF_6$ in acetonitrile, we once again carried out a controlled-potential oxidation under non-turnover conditions. The difference spectrum between the initial and final high-valent species revealed bleaches in absorption at 878, 860, and 835 cm^{-1} and increases in absorption at 851 and 844 cm^{-1} (Figure 4.9).

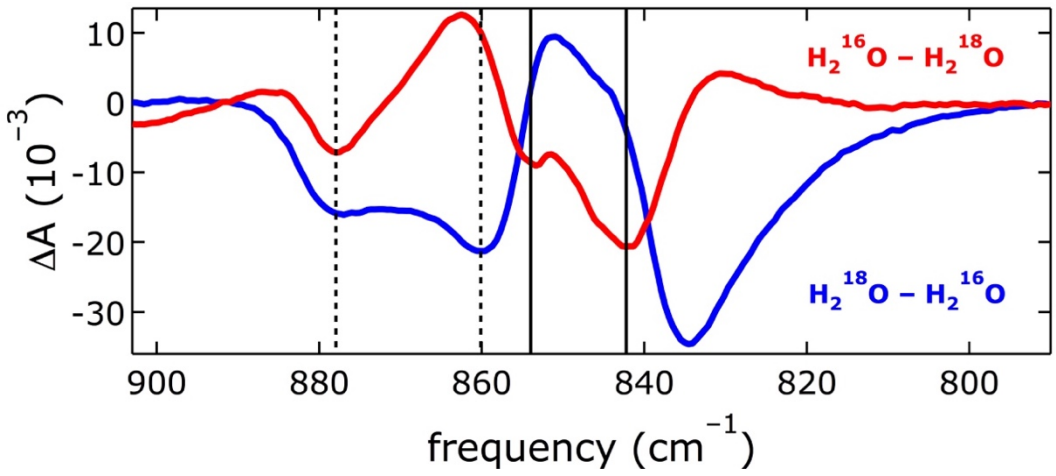

Figure 4.9. Partial isotope exchange experiment. Electrode was polarized at 2.3 V vs. Pt in acetonitrile, background taken, and quenched with 5% $H_2{}^{18}O$ in acetonitrile. Re-polarization at 2.3 V produced the blue trace ($H_2{}^{18}O$ – $H_2{}^{16}O$). A second background was taken and the electrode was quenched with 5% $H_2{}^{16}O$ in acetonitrile. Re-polarization at 2.3 V produced the red trace ($H_2{}^{16}O$ – $H_2{}^{18}O$).

Attempting to achieve full incorporation of ^{18}O into the active sites within the [NiFe]-LDH lattice, we carried out electrocatalytic water oxidation at a drop-cast film using $H_2{}^{18}O$, pH 14 for 30 minutes. We then transferred the modified electrode to the IR spectroelectrochemical cell, and performed a bulk oxidation (2.3 V *vs.* Pt, 0.1 M $[TBA]PF_6$ in acetonitrile) under non-catalytic conditions. The spectrum of the oxidized material was similar to that of the original high-valent species, but shifted by ~40 cm^{-1} to lower energy, consistent with complete exchange of ^{16}O with ^{18}O (Figure 4.5**D**). Due to the complete exchange, it is apparent that oxygen atoms are incorporated into the [NiFe]-LDH lattice during catalytic dioxygen evolution. These results strongly suggest that the sites we probed were directly involved in water oxidation. Notably, we found that the high-energy shoulder also was shifted by ~40 cm^{-1}, fully consistent with a side-bound peroxide[23].

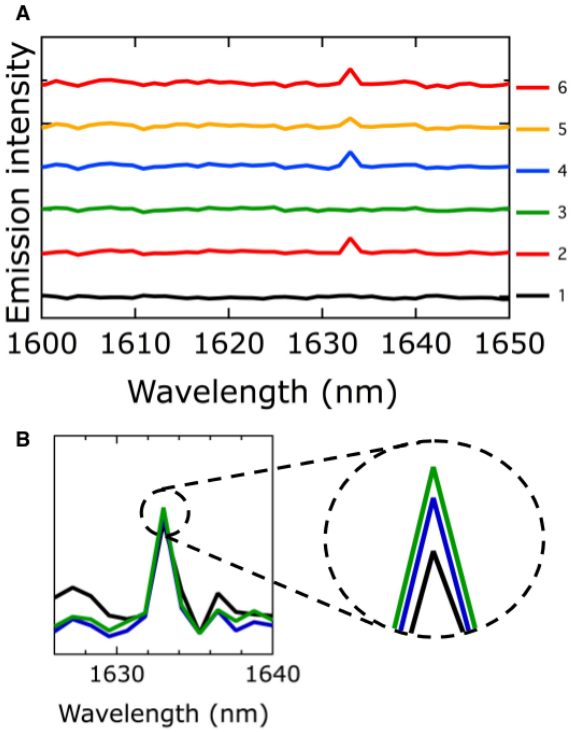

Figure 4.10. Near-infrared electrochemical luminescence measurements. (**A**) Controlled-potential steady-state luminescence cycled from (1) 0 V to (2) 2.3 V to (3) -0.5 V to (4) 2.3 V to (5) -0.5 V to (6) 2.3 V, all vs. a Pt wire pseudo-reference. (**B**) Time-course measurements of luminescence intensity at 1633 nm; 3 min. (black), 6 min. (blue), 9 min. (green).

4.2.4. Luminescence Spectroscopy

Tetraoxoferrate(VI) exhibits a narrow luminescence peak at ca. 6200 cm^{-1} (1613 nm), assigned to the $^1E \rightarrow {}^3A_2$ spin-flip transition[24]. We sought to detect an analogous Fe(VI) signature by spectroelectrochemical luminescence. Upon anodic polarization, a very narrow, weak signal appeared at 6124 cm^{-1} (1633 nm); the feature returned to baseline by biasing the electrode at -0.5 V. A second cycle reproduced the signal, although it did not entirely vanish under cathodic bias (Figure 4.10**A**(5)), consistent with features observed in the IR spectrum during redox cycling. Notably, the intensity of the luminescence increased with electrolysis time in a fashion similar to that of the infrared bands.

4.2.5. Oxygen Detection Studies/STOIR-O_2

To determine whether the species we were detecting spectroscopically was on the path to making oxygen, we sought to detect whether dioxygen was produced upon the addition of substrate (water).

We first performed bulk electrolyses in "wet" acetonitrile, with the addition of either 1% water or 1% 1 M KOH aqueous solution. The potential was set at 2.2 V vs Pt, and held until 2.5 x 10^{-2} C of charge was passed. The electrolyte solution was then assayed with an Amplex® Red hydrogen peroxide fluorescence assay (Figure 4.11). From the fluorescence intensity, we concluded that the high valent species produced hydrogen peroxide when quenched with water at pH 7, but no H_2O_2 was produced when quenched with water at pH 14.

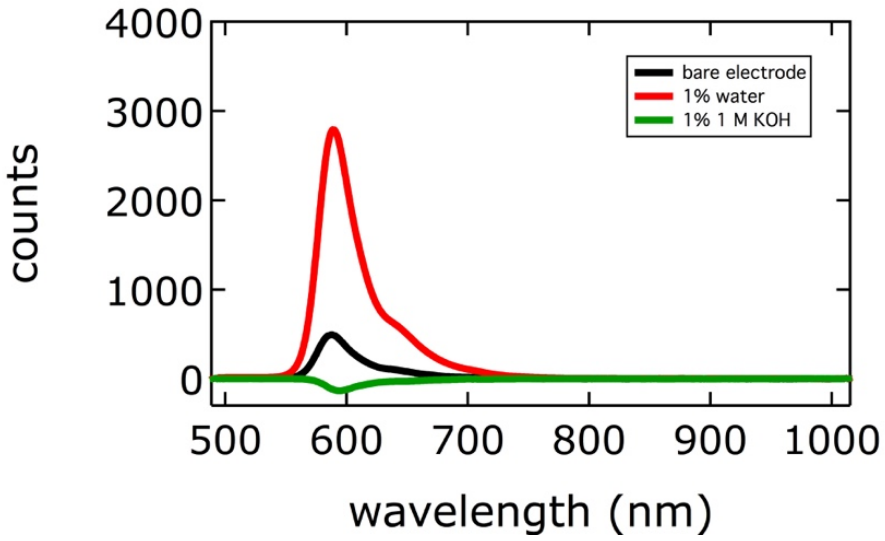

Figure 4.11. Steady-state fluorescence detection of hydrogen peroxide using Amplex® Red reagent. Fluorescence intensity is directly proportional to peroxide concentration. Fluorescence from the stock electrolyte solution has been subtracted, giving rise to a small "negative" region around 600 nm for the green trace.

To confirm that the oxidation product under alkaline conditions was O_2, we utilized an irreversible O_2-binding iridium complex, $Ir(dppe)_2Cl$ (dppe = 1,2-bis(diphenylphosphino)ethane)[25,26], to capture the small amount of O_2 produced upon quenching the polarized electrode. In this experiment, carbon fiber paper electrodes were transferred to an anaerobic optical cuvette containing $Ir(dppe)_2Cl$ in an alkaline acetonitrile solution (1% aqueous KOH, 1M), the spectrum of which had been recorded prior to exposure to the electrodes. Bleaching of the iridium complex absorption bands at 382, 442, and 512 nm indicated O_2 binding. We found that only electrodes containing catalyst that had been polarized at high potential (2 V *vs.* Pt) induced bleaching of the iridium absorption features. (Figures 4.12-4.15). Because the catalytic cycle was halted at the active species, this quenching experiment trapped a single turnover of O_2. In a typical experiment, we detected ~ 100 nmol of O_2, far greater than our detection limit. Based on the amount of oxygen produced, we estimate the number of active sites to be less than 5%. The failure of electrodes biased at lower potentials (*i.e.* 1 V *vs.* Pt) to produce O_2 indicated that the species we spectroscopically characterized was the *lowest potential intermediate active for water oxidation in non-aqueous media*.

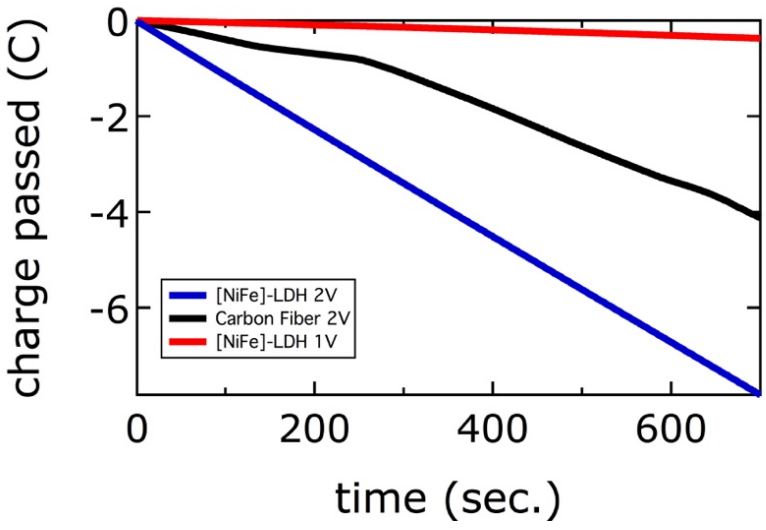

Figure 4.12. Chronocoulometric traces for STOIR-O_2 experiments.

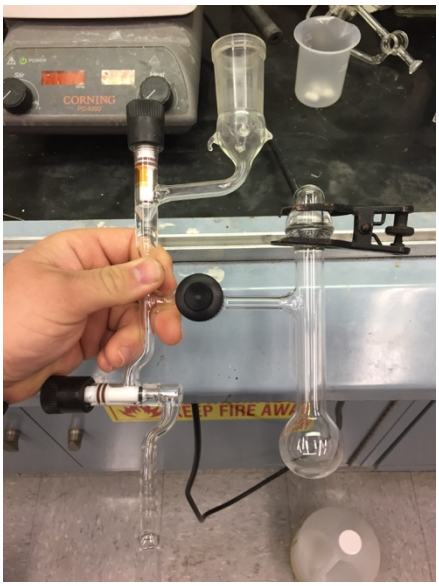

Figure 4.13. Custom laser cell for STOIR-O_2 experiments. Design allows the introduction of macroscopic carbon fiber electrodes while maintaining an oxygen-free atmosphere.

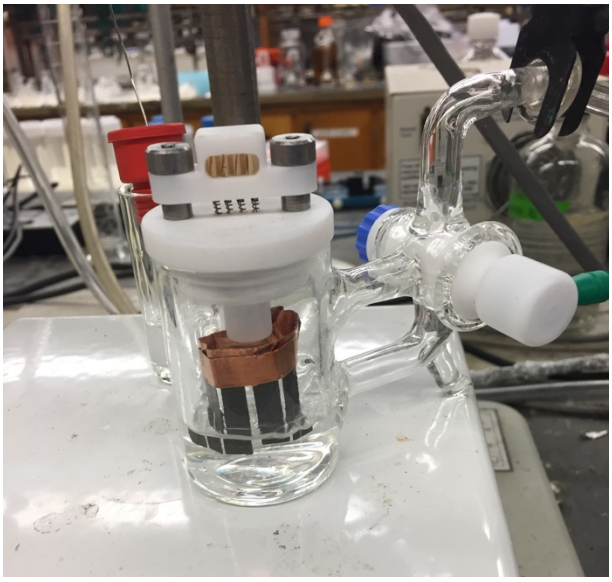

Figure 4.14. Electrochemical cell for STOIR-O_2 experiments. Electrodes are individual carbon fiber strips, held by copper tape.

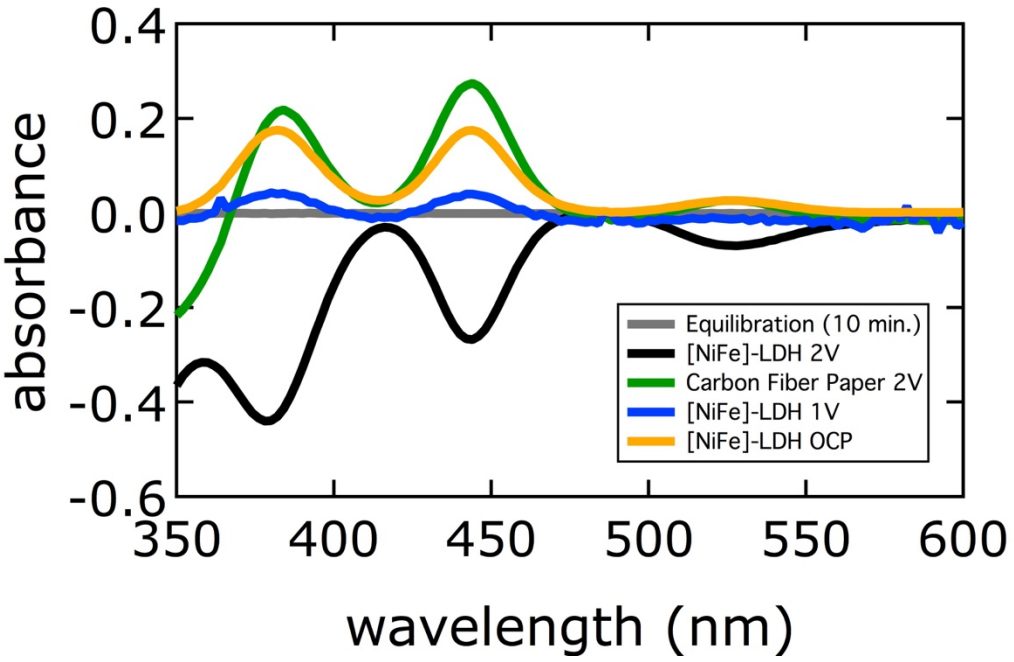

Figure 4.15. Spectra of $Ir(dppe)_2Cl$ in acetonitrile: 1% 1 M KOH, showing oxygen binding. Bleaches at 382, 442, and 512 nm are consistent with formation of an O_2 complex. Increased absorbance at those values indicate oxygen scrubbing from the solution, potentially due to oxygen deficiencies in the materials. Oxygen binding experiments were performed according to the procedure described in the text on carbon fiber electrodes polarized at: (black) 2 V *vs.* Pt (with catalyst); (green) 2 V *vs.* Pt (without catalyst); (blue) 1 V *vs.* Pt (with catalyst). A spectrum of the iridium complex in acetonitrile: 1% 1 M KOH for 10 minutes is shown in gray, and an oxygen binding experiment on the catalyst alone (no applied potential) is shown in orange.

4.2.6. Mössbauer Studies

We employed Mössbauer spectroscopy to probe the oxidation state of the high valent iron species observed at high potentials in nonaqueous media. These studies were performed on an ^{57}Fe enriched sample prepared by pulsed laser ablation in water. For nanoparticles in zero applied field the characteristic time for superparamagnetic relaxation is governed by the Néel-Brown relation,

$$\tau = \tau_0 \exp\left(\frac{E_a}{k_B T}\right),$$

where E_a is the barrier to flip the magnetization direction about the easy direction of magnetization. Thus, at very low temperatures the bulk Fe(III) will be in the slow relaxation limit ($\tau \gg 100$ ns), resulting in large internal magnetic fields and broadened, magnetically split spectra.[42] In order to be able to detect small quantities of Fe sites of catalytic relevance (~ 1-5 %), it is thus necessary to collect spectra at temperatures well above the average blocking temperature of the bulk material to obtain the narrowest possible linewidths. Given the temperature dependence of the Mössbauer-Lamb factor, this is most conveniently determined by measuring the maximum absorbance of the sample as function of temperature.

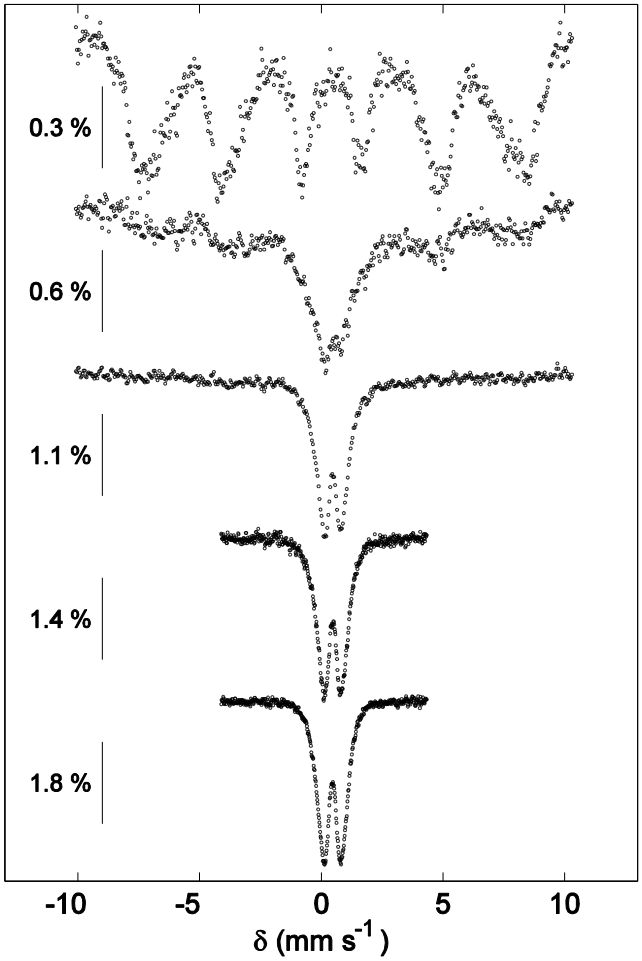

Figure 4.16. Temperature dependence of the Mössbauer signal of [Ni^{57}Fe]-LDH in zero applied field. From top to bottom, spectra were collected at 5, 15, 30, 50, and 80 K. The absorbance scale for each spectrum is indicated by the bar to the left.

As shown in Figure 4.16, we can estimate the rough blocking temperature of the bulk Fe(III) sites in the material around 15–30 K, below which the spectra display significant magnetic hyperfine splitting. Above 50 K, no resolved magnetic hyperfine splitting is observed in the spectra, but the linewidths continue to sharpen, indicative of a small percentage of very broad magnetically-split Fe(III) sites in the baseline. However, between

80 and 100 K, the maximum absorbance of the spectrum is reduced by 0.2% percent, suggesting a temperature regime where all of the Fe sites are in fast electronic relaxation.

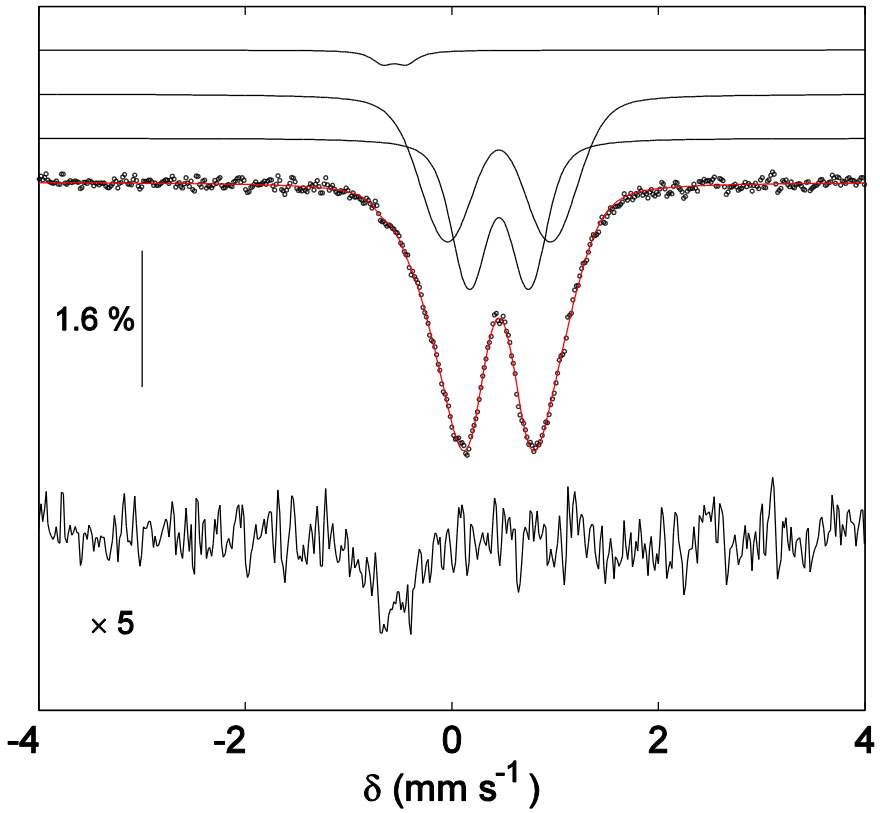

Figure 4.17. The zero field Mössbauer spectrum of [Ni^{57}Fe]-LDH collected at 100 K. The raw data are presented as open black circles, with the simulated spectrum shown in red. Individual sub-spectra are plotted as black lines above the raw data. Below is shown a subtraction of the simulated Fe(III) components from the data, showing the presence of a small amount of oxidized Fe present as a shoulder in the raw data.

The 100 K spectrum of an electrode polarized at high potential (Figure 4.17) consists of a doublet centered around 0.46 mm s^{-1}, with a clearly discernable shoulder appearing on the low energy resonance. The major signal is consistent with six-coordinate, high-spin Fe(III) in a ligand field of O-atom donors. As expected for a nanoparticle structure, the line shapes are not Lorentzian, but rather Voigt[27]. The Fe(III) signal was modeled using a

distribution of hyperfine parameters. To fully capture the observed shoulder, it was necessary to include a separate component in the simulation with $\delta = -0.51$ and $\Delta E_Q = 0.26$ mm s^{-1}. The low isomer shift of this component is consistent with the presence of a small amount (~ 2.5%) of Fe in an oxidation state greater than Fe(III)[28]. This isomer shift is also significantly more negative than that previously assigned to Fe(IV) in [NiFe]-LDH by *in-situ* Mössbauer (−0.27 mm s^{-1})[5]. Electrode polarization at lower potentials (*i.e.* 1 V *vs.* Pt) resulted in no Mössbauer spectroscopic features consistent with highly oxidized iron (Figure 4.18).

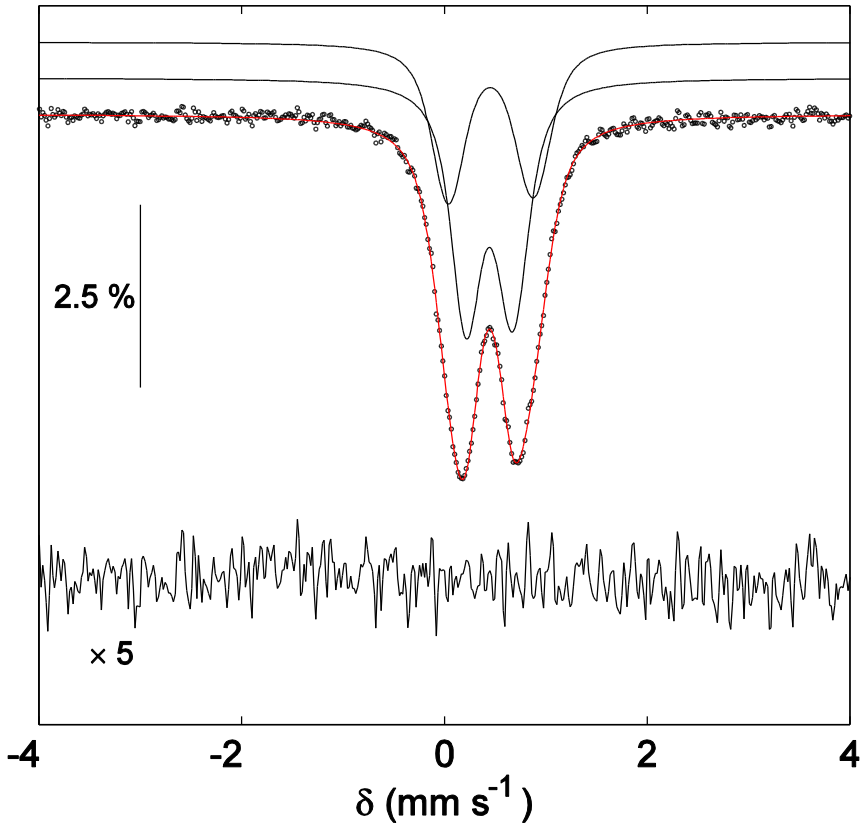

Figure 4.18. The zero field Mössbauer spectrum of [Ni^{57}Fe]-LDH, polarized at 1 V *vs.* Pt, collected at 100 K. The raw data are presented as open black circles, with the simulated spectrum shown in red. Individual sub-spectra are plotted as black lines above the raw data. Below is shown a subtraction of the simulated Fe(III) components from the data.

When a sample of catalyst initially polarized at 2 V *vs*. Pt (which showed the shoulder at $\delta = -0.51$ mm s^{-1}, described above) was removed from the spectrometer and wetted with 1% 1 M aqueous KOH in acetonitrile, the shoulder was no longer observed (Figure 4.19). Thus, the highly oxidized iron detected by Mössbauer was also incompatible (*i.e.* reactive) with aqueous base.

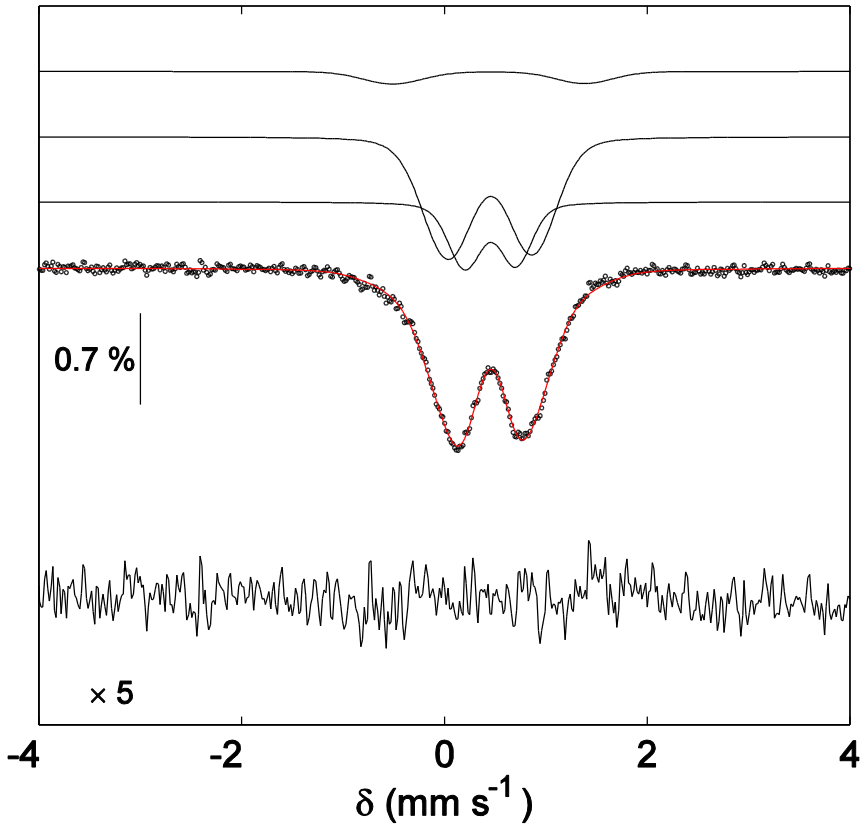

Figure 4.19. The zero field Mössbauer spectrum of [Ni^{57}Fe]-LDH, initially polarized at 2 V *vs.* Pt and then quenched in 1% 1 M aqueous KOH in acetonitrile, collected at 100 K. The raw data are presented as open black circles, with the simulated spectrum shown in red. Individual sub-spectra are plotted as black lines above the raw data. Below is shown a subtraction of the simulated Fe(III) components from the data.

We performed DFT calculations on single-site iron(VI) with three hydroxides and two oxos in which all atoms could be optimized; the apparent δ was calculated to be –0.68

mm s^{-1}. When the hydroxides were constrained to the lattice geometry, the isomer shift of Fe(VI) was calculated to be more positive, at –0.20 mm s^{-1}. A third calculation involving a 3-atom cluster of one Fe(VI) and two Al atoms yielded $\delta = -0.24$ mm s^{-1}. The computationally predicted limits for the isomer shift of iron(VI) in this environment, $-0.20 > \delta > -0.68$ mm s^{-1} (skewing more towards the negative), bound the experimentally observed isomer shift.

4.3. Mechanistic Proposal

The data are consistent with a catalytic cycle involving an Fe(VI) intermediate (Figure 4.20). Anodic bias brings the material to the so-called "γ-NiOOH" phase[29] in which Ni(III) predominates[30-34]. More positive potentials can lead either to formation of Ni(IV) or Fe(IV). Ni(IV), with a low-spin d^6 electronic configuration in octahedral coordination, cannot be stabilized by π-bonding to a terminal oxo-ligand. Fe(IV), however, with a d^4 configuration, has partially occupied $d\pi$-orbitals. In lattice sites where the Fe center has terminal hydroxide ligands, generation of the Fe(IV) state will be facilitated by deprotonation of this ligand to produce a terminal oxo. Hence, we anticipate that Fe centers in edge and corner sites are likely to be oxidized after formation of γ-NiOOH. Formation of Fe(IV)=O centers in the middle of the lattice would require disruption of triply bridging hydroxides, making the material susceptible to corrosion. Since the oxygen evolution reaction catalyzed by these materials in alkaline solution exhibits good long-term stability, we suggest that Fe(IV) formation occurs exclusively at edge and corner sites, which is compatible with the coulometry described above.

At slightly higher potentials, oxidation of Fe(IV)=O to Fe(V) or Fe(VI) occurs. These higher oxidation states can be stabilized by π-bonding to additional oxo-ligands. Only the corner sites in the LDH lattice have two or more terminal hydroxide ligands (Figure 4.1). The *trans*-dioxo geometry is preferred for a six-coordinate d^2 or d^3 metal center and neither corner site can adopt this configuration without lattice disruption.

Alternatively, reduction of the coordination number to 5 or 4 could stabilize a d^2 or d^3 configuration with *cis*-dioxo ligation. The 120° corner sites, which have just two terminal hydroxide ligands, could not reduce their coordination numbers without lattice disruption. The 60° corner sites, however, have three terminal hydroxide ligands, permitting formation of a 5-coordinate, *cis*-dioxo metal site; and in the Fe(VI) state, this 5-coordinate site would closely resemble ferrate. We note that others have proposed that tetrahedrally coordinated iron could be present under catalytic conditions[4].

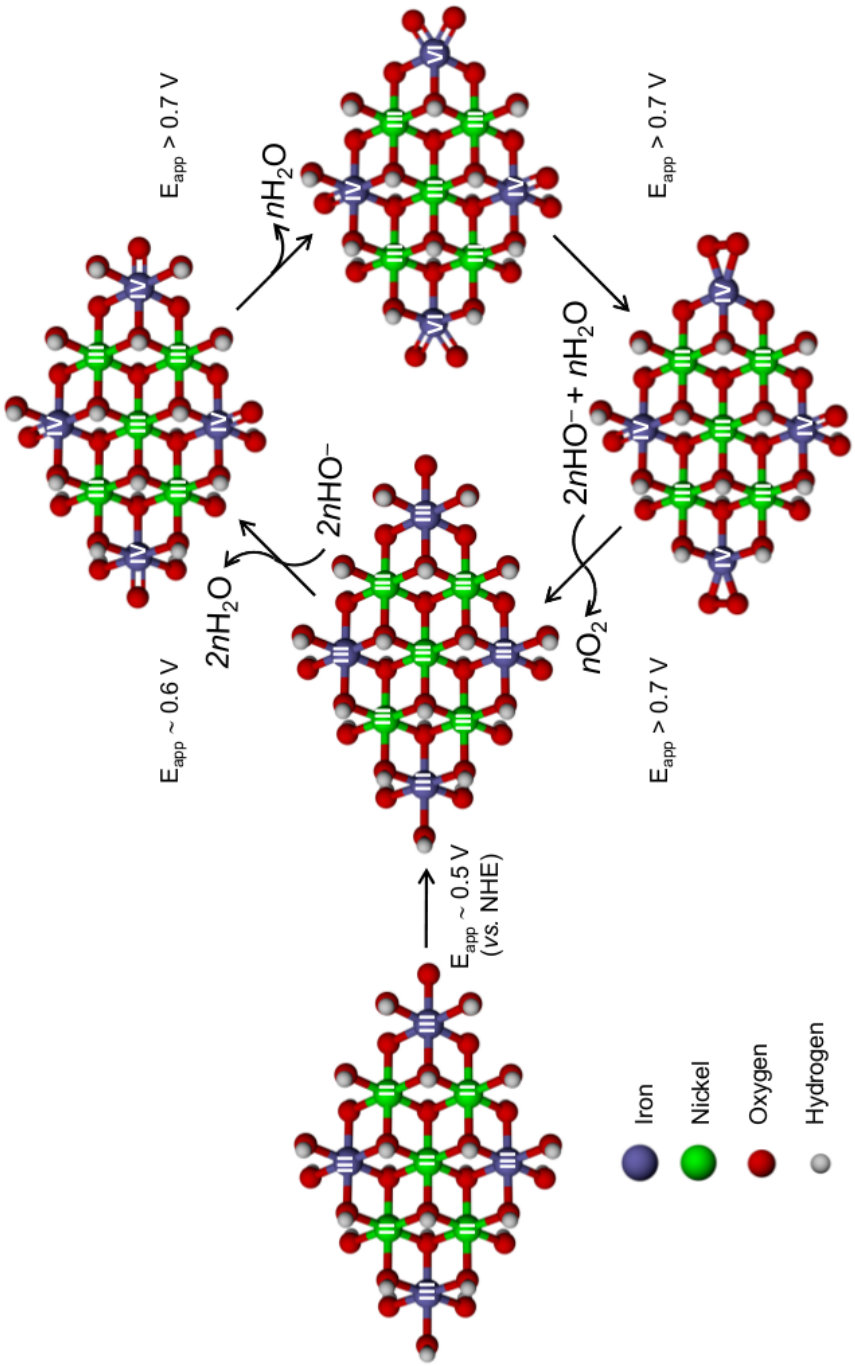

Figure 4.20. Proposed mechanism for water oxidation catalyzed by [NiFe]-LDH in alkaline solution. Oxidation states are shown as Roman numerals.

Internal redox rearrangement from a *cis*-dioxo-Fe(VI) species would produce an Fe(IV)-peroxide; the O-O stretch in this species is a plausible assignment for the high-energy peak in the infrared spectrum. Maintenance of the anodic bias, along with hydroxide binding leads to dioxygen release and reformation of γ-NiOOH. We note that ferrate and permanganate, both high-valent oxo-anions, are capable of forming O-O bonds. In our mechanism, the Ni(III) centers serve as a conduit for delivery of holes to the electrode. The high water oxidation activity of [NiFe]-LDH materials prepared by pulsed laser ablation in water may be related to the greater proportion of corner sites in nanosheets than in mesoscale materials.

Our mechanism is consistent with data on alkaline water oxidation by [NiFe]-LDH reported by other investigators. Strasser, Dau, and coworkers found a -120 mV/pH unit shift for the catalytic prewave in Ni-Fe catalysts, contrary to typical Nernstian behavior (-60 mV/pH unit) for the nickel-only material[35]. This behavior is consistent with a two proton-one electron transfer, cf. the *cis*-dioxo formation. Although Bell and coworkers concluded from X-ray absorption spectroscopy (XAS) that iron sites are not oxidized above the +3 oxidation state[4], their data are nevertheless consistent with a small amount of highly oxidized iron; at potentials effecting water oxidation *in operando*, a pronounced pre-edge appears (indicating significant *d-p* mixing) and the Fe K-edge shifts to higher energy. These trends have been observed in the XAS of potassium ferrate (K_2FeO_4), where the intensity of the pre-edge is a sensitive indicator of the oxidation state[36]. As the 1s to 3d transition is forbidden in centrosymmetric geometries, only iron in a non-octahedral or reduced coordination number environment would display such a pre-edge[37], and high-valent metal-oxo centers (*e.g.* d^2 for Fe(VI)) typically show intense pre-waves due to the short M-O bonds[38].

4.4. Conclusions

Our spectroscopic investigations in nonaqueous media suggest that nanostructuring by pulsed laser ablation in water gives a material with a high concentration of catalytic active sites. The nickel-hydroxide lattice provides a stable, corrosion-resistant host that tightly binds catalytic Fe centers, and the Ni(III)/(II) redox couple is ideally suited to the demands of water oxidation, providing both a reservoir of oxidizing equivalents and a conduit for transporting holes to the electrode. Importantly, only corner sites in the LDH lattice can accommodate the structural rearrangements necessary to produce the reactive *cis*-dioxo-Fe(VI) fragment.

4.5. Methods

Electrochemistry

Materials and procedures. [NiFe]-LDH was prepared by pulsed laser ablation in water, as described previously[1]. All measurements were performed in dried, degassed acetonitrile (HPLC grade, Fisher) that was passed through a solvent purification column. Tetra-*n*-butylammonium hexafluorophosphate ([TBA]PF_6) (Fluka) was used as received. Electrolyte solutions (0.1 M [TBA]PF_6) were prepared and stored over activated alumina and 4-Å molecular sieves.

All electrochemical experiments were performed with a CH Instruments Model 650A electrochemical analyzer. Cyclic voltammetry (CV) at ambient temperature was measured in a three-electrode configuration consisting of a highly polished glassy-carbon-disk working electrode (A = 0.07 cm^2), a Pt wire auxiliary electrode, and a 1.0 M KCl AgCl/Ag reference electrode, separated by a modified Luggin capillary. Potentials in the figures are reported vs. aqueous AgCl/Ag, not corrected for the junction potential. The ferricenium/ferrocene (Fc^+/Fc) potential was measured to be 410 mV under virtually identical conditions.

Electrodes were prepared by suspending 2 mg of [NiFe]-LDH in 1 mL of deionized water and sonicating for 15 minutes. To this suspension was added 20 μL of Nafion 117 solution (~5% in a mixture of lower aliphatic alcohols and water). The suspension was vortexed for 5 minutes. After polishing the electrode with 0.3 and 0.05 micrometer alumina successively, 20 μL of the [NiFe]-LDH was drop cast on the surface and allowed to dry under an infrared heat lamp for 20 minutes.

Small-Volume Electrolysis. A 1 cm diameter glassy carbon electrode was prepared by drop casting 80 μL of [NiFe]-LDH suspension and drying the electrode under an infrared heat lamp. Approximately 2 mL of 1 M aqueous KOH was placed in an evaporating dish and the electrode was positioned in the dish. The reference (1.0 M KCl AgCl/Ag reference electrode) was placed directly in the KOH electrolyte. A Pt wire counter electrode was in contact via a fritted glass tube.

Water oxidation was performed by passing 1 mA cm^{-2} (galvanostatic control) for 10 minutes, which turned the electrolyte purple.

The UV-visible spectrum of the resulting solution was recorded on an Ocean Optics USB 4000 spectrometer with an Ocean Optics USB-ISS-UV/VIS light source and SpectraSuite software.

Coulometry. We assume that the formula of the material is $Ni_{0.78}Fe_{0.22}(OH)_2(NO_3)_{0.22}$. Although it is known that carbonate substitutes for nitrate in aqueous base in ambient air[2], we assume that no ion exchange has occurred in acetonitrile. Further, we do not explicitly include interlayer water molecules, which we know are embedded in the interlayer from infrared spectroscopy[1].

Assuming the above formula, the MW is 105.72 g/mol. Depositing 20 μL of a 2 mg/mL solution, we expect to have 3.78×10^{-7} moles of Fe on the surface.

Infrared (IR) Spectroelectrochemistry

Infrared spectroelectrochemistry was carried out in diffuse reflectance mode using a custom-built cell.

Cell Design. The cell featured a 1 cm diameter circular glassy carbon electrode with a concentric (equidistant) platinum wire serving as a pseudo-reference electrode. The front window, made of zinc selenide (ZnSe, International Crystal Laboratories, 3 mm thick) was separated from the electrode by a 200 micrometer Teflon spacer. Inlet and outlet holes were plumbed with surgical tubing, with a platinum wire affixed to the outlet serving as an auxiliary electrode.

Electrode Preparation. A suspension of 2 mg [NiFe]-LDH in 1 mL of deionized water was made by sonicating for 15 minutes. For Nafion-containing electrodes, 20 μL of Nafion 117 solution were added to the suspension and it was vortexed for 5 minutes. Following polishing with 0.3 and 0.05 micrometer alumina, 80 μL of [NiFe]-LDH suspension was drop cast on the surface and allowed to dry under an infrared heat lamp for 15 minutes.

IR Measurements. Infrared absorption data were collected on a Thermo Nicolet Nexus FT-IR spectrometer using an LN_2-cooled MCT-A (Thermo) detector. The sample chamber was allowed to purge with nitrogen for one hour. A stand for the electrochemical cell was machined and two silver-deposited mirrors were used to guide light from the source onto the electrode surface (facing down), and reflected light to the detector. Beam alignment was performed using the spectrometer's internal He-Ne laser. A blank was recorded at no applied potential before the cell was switched on and potential was increased until maximum current flow was achieved (2.3 V vs. Pt). All spectra were background corrected.

Electrochemical Control. All potentiometric control was accomplished by a BAS model CV-27 electrochemical analyzer.

Solvent Control. Solvent flow was controlled using a gastight syringe connected to the input port of the spectroelectrochemical cell. Solvents were either acetonitrile (HPLC grade, Fisher) that had been passed through a solvent purification column and stored over activated alumina and molecular sieves, or nitromethane that had been distilled and sealed in glass ampules. Supporting electrolyte was 0.1 M tetrabutylammonium hexafluorophosphate.

For quenching experiments, a solution of 5% by weight water in acetonitrile was prepared.

Exhaustive Electrolysis in $H_2{}^{18}O$ Water. A pea-sized amount of solid potassium was added to ~20 mL of $H_2{}^{18}O$ and the pH was measured to be approximately 14. The spectroelectrochemical electrode was polarized, with the current held at 1 mA/cm^2 (galvanostatically). Oxygen bubbles were observed forming on the electrode. Electrolysis was continued for 10 minutes, after which the electrode was rinsed with deionized water and placed in the spectroelectrochemical cell. The cell was polarized *in-situ* at 2.3 V vs Pt. A high-frequency interference pattern due to the spacer thickness was removed by filtering the spectrum through a binomial smoothing algorithm with a smoothing parameter of 500. Notably, a ca. 10-fold loss in signal intensity was observed due to material coming off of the electrode surface.

Raman Spectroelectrochemistry

Raman spectroelectrochemistry was carried out in a custom-built cell.

Cell Design. The cell featured a 1 cm diameter circular glassy carbon electrode with a concentric (equidistant) platinum wire serving as a pseudo-reference electrode. The front window, made of fused silica (3 mm thick), was separated from the electrode by a 200 micrometer Teflon spacer. Inlet and outlet holes were plumbed with surgical tubing, with a platinum wire affixed to the outlet serving as an auxiliary electrode.

Electrode Preparation. A suspension of 2 mg [NiFe]-LDH in 1 mL of deionized water was made by sonicating for 15 minutes. Following polishing with 0.3 and 0.05 micrometer alumina, 80 μL of [NiFe]-LDH suspension was drop cast on the surface and allowed to dry under an infrared heat lamp for 15 minutes.

Raman Measurements. Raman data were collected on a Renishaw M1000 micro-Raman spectrometer using a 514.4 ± 0.3 nm excitation source (Cobolt Fandango 100 laser) at 10% power. A 50x long working distance objective was used. The excitation source was focused on the material deposited on the electrode, and the Raman signal (absent potential) was shown to match the Raman spectra of the as-prepared catalyst[1].

Electrochemical Control. All potentiometric control was accomplished by a CH Instruments Model 650A electrochemical analyzer.

Solvent Control. Solvent flow was controlled using a gastight syringe connected to the input port of the spectroelectrochemical cell. Solvents were either acetonitrile (HPLC grade, Fisher) that had been passed through a solvent purification column and stored over activated alumina and molecular sieves, or nitromethane that had been distilled and sealed in glass ampules. Supporting electrolyte was 0.1 M tetrabutylammonium hexafluorophosphate.

UV-Visible (UV-vis) Spectroelectrochemistry

UV-vis spectroelectrochemistry was carried out in specular reflectance mode using a custom-built cell.

Cell Design. The cell featured a 1 cm diameter circular glassy carbon electrode with a concentric (equidistant) platinum wire serving as a pseudo-reference electrode. The front window, made of fused silica (3 mm thick), was separated from the electrode by a 200 micrometer Teflon spacer. Inlet and outlet holes were plumbed with surgical tubing, with a platinum wire affixed to the outlet serving as an auxiliary electrode.

Electrode Preparation. A suspension of 2 mg [NiFe]-LDH in 1 mL of deionized water was made by sonicating for 15 minutes. Following polishing with 0.3 and 0.05 micrometer alumina, 80 μL of [NiFe]-LDH suspension was drop cast on the surface and allowed to dry under an infrared heat lamp for 15 minutes.

UV-Vis Measurements. An Ocean Optics UV-vis light source (DH-2000) and spectrometer (USB2000) were connected to the Y-arms of a bifurcated fiber-optic cable; the end of the cable was connected through a lens housing containing a semi-spherical collimating lens to the front-face window of the spectroelectrochemical cell at a 90 degree angle. A drop of mineral oil between the fiber optic and front-face fused silica window of the cell ensured refractive-index matching. Spectra were not corrected for front-face reflection. The error in intensity at an absorbance of 0.5 was less than 1%.

Electrochemical Control. All potentiometric control was accomplished using a CH Instruments Model 650A electrochemical analyzer.

Solvent Control. Solvent flow was controlled using a gastight syringe connected to the input port of the spectroelectrochemical cell. The solvent was acetonitrile (HPLC grade,

Fisher) that had been passed through a solvent purification column and stored over activated alumina and molecular sieves. Supporting electrolyte was 0.1 M tetrabutylammonium hexafluorophosphate.

Chemical Oxidation by Hydrogen Peroxide. To a suspension of 2 mg [NiFe]-LDH suspended in 1 mL of deionized water was added 100 μL of 30% hydrogen peroxide solution. The solution was placed in front of a mercury vapor lamp for 10 minutes to stimulate the production of hydroxyl radical. The UV-visible spectrum was recorded on an Ocean Optics USB 4000 spectrometer with an Ocean Optics USB-ISS-UV/VIS light source and SpectraSuite software.

Spectrum of Potassium Ferrate. Potassium ferrate was prepared as described previously[30]. The UV-visible spectrum was recorded on an Ocean Optics USB 4000 spectrometer using the SpectraSuite software. The pH was 7.

Density Functional Theory (DFT) Calculations

The structure of the ferrate (FeO_4^{2-}) anion was optimized using the Orca program package[31] with the PBE0 functional and Ahlrichs VDZ basis set[32]. The full Hessian was then calculated and the vibrational frequencies were read from the output file.
Infrared and Raman spectra were calculated using the orca_mapspc tool with 15 cm^{-1} FWHM values.

Mössbauer shifts were calculated using the method of Neese with the B3LYP functional and the CP(PPP) basis on iron, which gives the best correlation to experimental parameters for 20 control complexes, including ferrate (FeO_4^{2-})[33].

Control Experiments with "Wet" Acetonitrile

Water Oxidation. A 1 cm diameter glassy carbon electrode was prepared by drop casting 80 μL of [NiFe]-LDH suspension and drying the electrode under an infrared heat lamp. A typical three-electrode cell was used. The reference (1.0 M KCl AgCl/Ag reference electrode) compartment was separated from the working compartment by a Luggin capillary. A Pt wire counter electrode was in contact via a coarse frit. The cell was stirred.

Electrolyte was either 0.1 M tetrabutylammonium hexafluorophosphate in acetonitrile with 1% water, or 0.1 M tetrabutylammonium hexafluorophosphate in acetonitrile with 1% 1 M aqueous KOH. The working electrode potential was held constant and 2.5×10^{-2} C of charge was passed. Time elapsed was 970 seconds (bare electrode, no catalyst), 229 seconds (catalyst in 1% water) and 225 seconds (catalyst in 1% 1 M aqueous KOH).

Hydrogen Peroxide Assay. An Amplex® Red Hydrogen Peroxide/Peroxidase Assay Kit was obtained from ThermoFisher. A working solution of 100 μM Amplex® Red reagent and 0.2 U/mL HRP was prepared immediately prior to quantification. Equal volumes (1 mL) of electrolyte and working solution were mixed and incubated in the dark for 30 minutes.

Steady-State Fluorescence. Steady-state fluorescence profiles were obtained with 488.0 nm excitation (Coherent Innova 70 argon-ion laser). Luminescence was collected using an optical fiber optic and directed to a Melles Griot 13 FOS 200 spectrometer. A 488.0 nm long-pass cutoff filter was used to reject excitation light.

Luminescence Spectroelectrochemistry

Luminscence spectroelectrochemistry was carried out in specular reflectance mode using a custom-built cell.

Cell Design. The cell featured a 1 cm diameter circular glassy carbon electrode with a concentric (equidistant) platinum wire serving as a pseudo-reference electrode. The front window, made of fused silica (3 mm thick), was separated from the electrode by a 100 micrometer Teflon spacer. Inlet and outlet holes were plumbed with surgical tubing, with a platinum wire affixed to the outlet serving as an auxiliary electrode.

Electrode Preparation. A suspension of 2 mg [NiFe]-LDH in 1 mL of deionized water was made by sonicating for 15 minutes. Following polishing with 0.3 and 0.05 micrometer alumina, 80 μL of [NiFe]-LDH suspension was drop cast on the surface and allowed to dry under an infrared heat lamp for 15 minutes.

Luminescence Measurements. A 20 W Oriel Quartz Tungsten Halogen (QTH) lamp was coupled to the 100 μm-core arm of a bifurcated optical fiber. The 200 μm-core common

end of the cable was connected through a lens housing containing a semi-spherical collimating lens to the front-face window of the spectroelectrochemical cell at a 90 degree angle. The remaining 100 μm-core arm was coupled to a NIR-grade fiber bundle (10 fibers, 200 μm each) by an SMA-to-SMA coupler. The fiber bundle terminated in a linear array which directly coupled to an EG&G Princeton Applied Research Model 1235 digital triple grating spectrograph with 275 mm focal length. The detector was an EG&G Princeton Applied Research Model 1452 NIR InGaAs-InP alloy 256-element linear array. The detector was cooled to 2°C. The grating had 150 grooves/mm and was blazed at 1250 nm. The system had about 3 nm resolution in the 1600 nm region of the NIR. Integration time was 1.5 seconds per scan, and 50 scans were integrated per spectrum. In order to collect the entire region from 1100-1700 nm, a single grating change was made in the middle of acquisition, resulting in a total scan time of 2.5 minutes, plus time spent communicating with the console.

A light leakage scan was taken at 1.5 seconds integration time; this signal was subsequently subtracted from all obtained spectra. The data presented is the ratio of counts obtained under potential to counts obtained before electrolysis.

Electrochemical Control. All potentiometric control was accomplished using a CH Instruments Model 650A electrochemical analyzer.

Solvent Control. Solvent flow was controlled using a gastight syringe connected to the input port of the spectroelectrochemical cell. The solvent was acetonitrile (HPLC grade, Fisher) that had been passed through a solvent purification column and stored over activated alumina and molecular sieves. Supporting electrolyte was 0.1 M tetrabutylammonium hexafluorophosphate.

Oxygen Detection Experiments

Synthesis of Vaska's Complex—Step 1: Chlorobis(cyclooctene)iridium(I)dimer (Sigma-Aldrich) was dissolved in acetonitrile. The solution was stirred at room temperature for 10 minutes under argon. The argon flow was then stopped and CO gas was passed through the solution until a green color was observed. Four equivalents of PPh_3 were added in dichloromethane and the solution was stirred for 30 minutes as a yellow precipitate formed.

The solvent was evaporated under vacuum and the precipitate was washed with diethyl ether. The "tennis ball yellow" compound was recrystallized from DCM/hexane and stored under argon.

Synthesis of Ir(dppe)$_2$Cl—Step 2: Standard procedure was followed[25]. Briefly, two equivalents of dppe (dppe = 1,2-bis(diphenylphosphino)ethane) in benzene were added to Vaska's complex (also in benzene) under argon and stirred until a white precipitate formed. The carbonyl is then removed by heating the white solid to 100°C in a 10:1 mixture of toluene:1-propanol. The bright orange precipitate is the irreversible O_2 binding complex.

Oxygen Binding Experiments: A solution of acetonitrile with 1% 1 M aqueous KOH was thoroughly degassed by a free-pump-thaw method in a modified laser cell bulb and isolated in the cuvette. Approximately 20 mg of Ir(dppe)$_2$Cl was added to the bulb and cycled with vacuum and argon at least 10 times. The solution and the complex were mixed and a background spectrum was taken. The solution was then isolated in the cuvette. While isolated, the remainder of the cell was rinsed with acetone to ensure no complex remained; the cell was then dried under vacuum for 15 minutes to remove any remaining acetone.

Electrolysis: Five carbon fiber paper electrodes, 0.5 cm x 2 cm, were soaked in a 2 mg/1 mL suspension of [NiFe]-LDH in water for 10 minutes. The electrodes were then placed into a three-compartment electrochemical cell, supported by copper tape. The electrodes were held at 2 V *vs.* Pt for 1000 seconds before being removed and immediately dropped into the bulb of the laser cuvette (above). The bulb was cycled with vacuum and argon at least 10 times.

Spectroscopy: The solution and electrodes were "mixed" briefly (about 30 seconds), and a spectrum of the solution was taken, referenced to the background taken initially. Spectra were compared to prior studies of O_2 adducts of this complex[26].

Mössbauer Spectroscopy

Mössbauer spectra were recorded on a spectrometer from SEE Co. (Edina, MN) operating in the constant acceleration mode in a transmission geometry in zero applied magnetic field. The sample was kept in an SVT-400 cryostat form Janis (Wilmington, MA),

using either liquid He (for temperatures < 80 K) or liquid N_2 (for temperatures > 80 K) as a cryogen. The quoted isomer shifts are relative to the centroid of the spectrum of a metallic foil of α-Fe at room temperature. Samples were prepared by polarizing carbon fiber paper soaked in [Ni^{57}Fe]-LDH suspension, removing the electrodes under potential, and punching holes directly into liquid nitrogen. The frozen punches were then mounted into a Delrin cup fitted with a screw-cap. Data analysis was performed using version 4 of the program WMOSS (www.wmoss.org).

As is typical for Fe-containing nanoparticles, the Lorentzian line shape required for a single Fe absorber is not observed in the Mössbauer spectra. Rather, a distribution of local Fe environments exists in the material, resulting in a distribution of hyperfine interactions[27,42]. In the limit of fast electronic relaxation, internal fields average to zero and a distribution of quadrupole doublets is obtained. It is assumed that the quadrupole splittings are normally distributed according to,

$$P\left(\Delta E_Q\right) = \sum_{i=1}^{N} p_i G_i(\Delta E_Q),$$

where $G\left(\Delta E_Q\right)$ is Gaussian with normalization constant p_i. Assuming the isomer shifts are linearly coupled to the quadrupole splitting, the elementary quadrupole doublet is then given by,

$$D(v) = \sum_{k=-1}^{1} h_k \frac{\frac{\gamma^2}{4}}{\left(v-\delta_0-\delta_1\Delta E_Q-k\Delta E_Q/2\right)^2+\frac{\gamma^2}{4}},$$

where h_k is the Lorentzian height, γ is the width, and v is velocity. The observed spectrum is then,

$$f(v) = \int D(v)P\left(\Delta E_Q\right)d\Delta E_Q,$$

equivalent to a sum of $2N$ Voigt lineshapes. To simulate the data, the number of distributions N was gradually increased until the fitting parameters $(\gamma, \delta_0, \delta_1, h_1/h_{-1})$ became stable.

In the 100 K spectrum of [Ni^{57}Fe]-LDH polarized at 2 V *vs.* Pt, a shoulder appeared at around −0.5 mm s^{-1}. Attempting to fit this feature as an additional Fe(III) component with δ = 0.3–0.5 mm s^{-1} improved the fit marginally, but did not qualitatively capture the observed

shoulder. However, as shown in Table S-2, inclusion of a component with negative isomer shift led to a substantial improvement of the simulation.

DFT Calculations: Mössbauer shifts were calculated using the method of Neese with the B3LYP functional and the CP(PPP) basis on iron, which gave the best correlation to experimental parameters for 20 control complexes, including ferrate (FeO_4^{2-})[43].

Table 4-2: Simulation for [Ni^{57}Fe]-LDH polarized at 2 V *vs.* Pt, at 100 K using a hyperfine distribution model.

	Parameters			
	***N* = 1**	***N* = 2**	***N* = 3**	**Final fit**
$\Delta E_{Q,1}$ (mm s^{-1})	0.791	0.619	0.590	0.498
σ_1 (mm s^{-1})	0.578	0.520	0.549	0.366
p_1 (mm s^{-1})	1.078	0.546	0.603	0.305
$\Delta E_{Q,1}$ (mm s^{-1})		1.098	1.095	0.852
σ_1 (mm s^{-1})		0.956	0.576	0.648
p_1 (mm s^{-1})		0.487	0.299	0.534
$\Delta E_{Q,1}$ (mm s^{-1})			1.619	1.345
σ_1 (mm s^{-1})			0.910	0.821
p_1 (mm s^{-1})			0.125	0.173
γ (mm s^{-1})	0.431	0.267	0.228	0.250
δ_0 (mm s^{-1})	0.487	0.474	0.472	0.457
δ_1 (mm s^{-1})	−0.042	−0.028	−0.025	−0.022
h_1/h_{-1}	0.963	0.955	0.954	1.005
δ (mm s^{-1})				-0.511
ΔE_Q (mm s^{-1})				0.262
γ (mm s^{-1})				0.250
Area				0.024
Red. χ^2	1.740	0.682	0.615	0.567

Table 4-3: Simulation for [Ni^{57}Fe]-LDH, polarized at 1 V *vs.* Pt, at 100 K using a hyperfine distribution model.

	Parameters	
	***N* = 1**	***N* = 2 (Final)**
$\Delta E_{Q,1}$ (mm s^{-1})	0.606	0.470
σ_1 (mm s^{-1})	0.559	0.350
p_1 (mm s^{-1})	0.997	0.608
$\Delta E_{Q,1}$ (mm s^{-1})		0.853
σ_1 (mm s^{-1})		0.430
p_1 (mm s^{-1})		0.384
$\Delta E_{Q,1}$ (mm s^{-1})		
σ_1 (mm s^{-1})		
p_1 (mm s^{-1})		
γ (mm s^{-1})	0.297	0.277
δ_0 (mm s^{-1})	0.423	0.430
δ_1 (mm s^{-1})	0.041	0.030
h_1/h_{-1}	1.015	1.005
Red. χ^2	0.910	0.591

Table 4-4: Simulation for [Ni^{57}Fe]-LDH, after quenching, at 100 K using a hyperfine distribution model.

	Parameters		
	***N* = 1**	***N* = 2**	***N* = 3 (Final)**
$\Delta E_{Q,1}$ (mm s^{-1})	0.737	0.606	0.503
σ_1 (mm s^{-1})	0.568	0.616	0.610
p_1 (mm s^{-1})	1.044	0.497	0.243
$\Delta E_{Q,1}$ (mm s^{-1})		0.977	0.834
σ_1 (mm s^{-1})		1.116	1.011
p_1 (mm s^{-1})		0.485	0.650
$\Delta E_{Q,1}$ (mm s^{-1})			1.888
σ_1 (mm s^{-1})			1.228
p_1 (mm s^{-1})			0.081
γ (mm s^{-1})	0.423	0.224	0.133
δ_0 (mm s^{-1})	0.462	0.465	0.460
δ_1 (mm s^{-1})	−0.015	−0.020	−0.013
h_1/h_{-1}	0.930	0.915	0.922
Red. χ^2	0.854	0.608	0.562

4.6. References and Notes

1. Hunter, B. M. *et al*. Highly Active Mixed-Metal Nanosheet Water Oxidation Catalysts Made by Pulsed-Laser Ablation in Liquids. *J. Am. Chem. Soc*. **136**, 13118-13121 (2014).

2. Hunter, B. M., Hieringer, W., Winkler, J. R., Gray, H. B. & Müller, A. M. Effect of interlayer anions on [NiFe]-LDH nanosheet water oxidation activity. *Energy Environ. Sci*. **9**, 1734-1743 (2016).

3. Blakemore, J. D., Gray, H. B., Winkler, J. R. & Müller, A. M. Co_3O_4 Nanoparticle Water-Oxidation Catalysts Made by Pulsed-Laser Ablation in Liquids. *ACS Catal*. **3**, 2497-2500 (2013).

4. Friebel, D. *et al*. Identification of Highly Active Fe Sites in (Ni,Fe)OOH for Electrocatalytic Water Splitting. *J. Am. Chem. Soc*. **137**, 1305-1313 (2015).

5. Chen, J. Y. C. *et al*. Operando Analysis of NiFe and Fe Oxyhydroxide Electrocatalysts for Water Oxidation: Detection of Fe^{4+} by Mössbauer Spectroscopy. *J. Am. Chem. Soc*. **137**, 15090-15093 (2015).

6. Ahn, H. S. & Bard, A. J. Surface Interrogation Scanning Electrochemical Microscopy of $Ni_{1-x}Fe_xOOH$ ($0 < x < 0.27$) Oxygen Evolving Catalyst: Kinetics of the "fast" Iron Sites. *J. Am. Chem. Soc*. **138**, 313-318 (2016).

7. Görlin, M. *et al*. Oxygen Evolution Reaction Dynamics, Faradaic Charge Efficiency, and the Active Metal Redox States of Ni–Fe Oxide Water Splitting Electrocatalysts. *J. Am. Chem. Soc*. **138**, 5603-5614 (2016).

8. Hunter, B. M., Gray, H. B. & Müller, A. M. Earth-Abundant Heterogeneous Water Oxidation Catalysts. *Chem. Rev*. **116**, 14120-14136 (2016).

9. The [NiAl]-LDH was prepared by precipitation synthesis, resulting in much larger particles than the [NiFe]-LDH prepared by pulsed laser ablation in water. As a result, suspensions of the "nickel-only" material were prone to settling and electrode coatings were much lower. This was reflected both visibly in the electrode coverage and in the current observed in the cyclic voltammograms.

10. For [NiFe]-LDH, we observe a catalytic water oxidation current of 10 mA cm^{-2} at ~0.660 V *vs*. NHE in 1 M aqueous KOH (pH 14). In an attempt to compare this potential to the potentials measured in acetonitrile, one can correct for pH, water content of the acetonitrile solvent, and liquid-liquid junction potentials. The cathodic shift of the acetonitrile potentials to a pseudo aqueous NHE reference is estimated to be within 300 mV of the observed catalytic current in aqueous alkaline solution.

11. Huynh, M. H. V. & Meyer, T. J. Proton-Coupled Electron Transfer. *Chem. Rev.* **107**, 5004-5064 (2007).

12. The initial, “background” spectrum was recorded at an applied potential of 1.5 V—i.e., positive of the Ni-centered oxidations.

13. The potential, relative to a platinum wire, was increased until maximum current was passed, indicating that the oxidation events in the cyclic voltammogram had been reached. This occured at 2.3 V *vs*. the Pt pseudo-reference.

14. In control experiments where water oxidation was carried out in acetonitrile with 1% water or 1% 1 M aqueous KOH, the former produced a large quantity of hydrogen peroxide, whereas the latter produced an undetectable amount of hydrogen peroxide. We conclude that the product of quenching with 1% 1 M aqueous KOH in acetonitrile is dioxygen (see SI).

15. Proshlyakov, D. A., Henshaw, T. F., Monterosso, G. R., Ryle, M. J. & Hausinger, R. P. Direct Detection of Oxygen Intermediates in the Non-Heme Fe Enzyme Taurine/α-Ketoglutarate Dioxygenase. *J. Am. Chem. Soc.* **126**, 1022-1023 (2004).

16. Busca, G. Differentiation of mono-oxo and polyoxo and of monomeric and polymeric vanadate, molybdate and tungstate species in metal oxide catalysts by IR and Raman spectroscopy. *J. Raman. Spectrosc.* **33**, 348-358 (2002).

17. Xiao, Z., Gable, R. W., Wedd, A. G. & Young, C. G. Complexes Containing *cis*-$[Mo^{V}O_2]^{+}$ and *cis*-$[Mo^{V}O(OH)]^{2+}$ Centers. *J. Am. Chem. Soc.* **118**, 2912-2921 (1996).

18. Bridgeman, A. J. & Cavigliasso, G. Molecular and electronic structures of six-coordinate chloro-oxo-metalate complexes of V, Nb, Ta, Mo, and W. *J. Chem. Soc., Dalton Trans.*, 3556-3563 (2001).

19. Griffith, W. P. & Wickins, T. D. *cis*-Dioxo- and trioxo-complexes. *J. Chem. Soc. A*, 400-404 (1968).

20. We were initially surprised that a purple substance occasionally leached out of the material during in-situ infrared experiments. Under (aqueous) turnover conditions, we were reproducibly able to turn the electrolyte purple by operating the cell in a small volume of water. As the pH near the electrode dropped (due to the water oxidation half-reaction), we believe that the LDH material became unstable and Fe(VI) leached out, leading to a purple solution. The UV-visible spectrum of the resulting solution is similar to that of potassium ferrate in solution (SI). Interestingly, in-situ UV-visible spectroelectrochemical oxidation of drop cast films in 0.1 M $[TBA]PF_6$/acetonitrile showed two analogous bands (at ~500 and ~600 nm) for surface-confined species, similar to the spectrum of potassium ferrate in solution (SI).

21. Burke, M. S., Kast, M. G., Trotochaud, L., Smith, A. M. & Boettcher, S. W. Cobalt–Iron (Oxy)hydroxide Oxygen Evolution Electrocatalysts: The Role of Structure and Composition on Activity, Stability, and Mechanism. *J. Am. Chem. Soc.* **137**, 3638-3648 (2015).

22. Zou, S. *et al.* Fe (Oxy)hydroxide Oxygen Evolution Reaction Electrocatalysis: Intrinsic Activity and the Roles of Electrical Conductivity, Substrate, and Dissolution. *Chem. Mater.* **27**, 8011-8020 (2015).

23. Liang, H.-C. *et al.* Contrasting Copper–Dioxygen Chemistry Arising from Alike Tridentate Alkyltriamine Copper(I) Complexes. *J. Am. Chem. Soc.* **124**, 4170-4171 (2002).

24. Brunold, T. C., Hauser, A. & Güdel, H. U. Absorption and luminescence spectroscopy of ferrate (VI) doped into crystals of K_2MO_4 (M = S, Se, Cr, Mo). *J. Lumin.* **59**, 321-332 (1994).

25. Vaska, L., Catone, D. L. A New Series of Four-, Five-, and Six-Coordinated Iridium Complexes. *J. Am. Chem. Soc.* **88**, 5324-5325.

26. Geoffroy, G. L., Hammond, G. S., Gray, H. B. Photochemical Reductive Elimination of Oxygen, Hydrogen, and Hydrogen Chloride from Iridium Complexes. *J. Am. Chem. Soc.* **97**, 3933-3936.

27. Rancourt, D. G.; Ping, J. Y. *Nuclear Instruments and Methods in Physics Research Section B: Beam Interactions with Materials and Atoms* **1991,** *58*, 85-97.

28. The significantly higher percentage of electroactive iron in this experiment (3% *vs.* 0.0002% found previously) was due to the high surface area of the electrode material, carbon fiber paper rather than glassy carbon.

29. Klaus, S., Cai, Y., Louie, M. W., Trotochaud, L. & Bell, A. T. Effects of Fe Electrolyte Impurities on $Ni(OH)_2$/NiOOH Structure and Oxygen Evolution Activity. *J. Phys. Chem. C* **119**, 7243-7254 (2015).

30. Lyons, M. D. & Brandon, M. P. The Oxygen Evolution Reaction on Passive Oxide Covered Transition Metal Electrodes in Aqueous Alkaline Solution. Part 1-Nickel. *Int. J. Electrochem. Sci.*, 1386-1424 (2008).

31. Desilvestro, J., Corrigan, D. A. & Weaver, M. J. Characterization of Redox States of Nickel Hydroxide Film Electrodes by In Situ Surface Raman Spectroscopy. *J. Electrochem. Soc.* **135**, 885-892 (1988).

32. Oliva, P. *et al*. Review of the structure and the electrochemistry of nickel hydroxides and oxy-hydroxides. *J. Power Sources* **8**, 229-255 (1982).

33. Barnard, R., Randell, C. F. & Tye, F. L. Studies concerning charged nickel hydroxide electrodes I. Measurement of reversible potentials. *J. Appl. Electrochem.* **10**, 109-125 (1980).

34. Doyle, R. L., Godwin, I. J., Brandon, M. P. & Lyons, M. E. G. Redox and electrochemical water splitting catalytic properties of hydrated metal oxide modified electrodes. *PCCP* **15**, 13737-13783 (2013).

35. Görlin, M. *et al*. Tracking Catalyst Redox States and Reaction Dynamics in Ni—Fe Oxyhydroxide Oxygen Evolution Reaction Electrocatalysts: The Role of Catalyst Support and Electrolyte pH. *J. Am. Chem. Soc.* **139**, 2070-2082 (2017).

36. Farmand, M. *et al*. Super-iron nanoparticles with facile cathodic charge transfer. *Electrochem. Commun.* **13**, 909-912 (2011).

37. Farmand, M., Licht, S. & Ramaker, D. Studying the Reversibility of Multielectron Charge Transfer in Fe(VI) Cathodes Utilizing X-ray Absorption Spectroscopy. *J. Phys. Chem. C* **117**, 19875-19884 (2013).

38. Chandrasekaran, P. *et al*. Prediction of High-Valent K-edge Absorption Spectra by Time-Dependent Density Functional Theory. *Dalton Trans*. **40**, 11070-11079 (2011).

39. Caddick, S., Murtagh, L. & Weaving, R. Potassium Ferrate on Wet Alumina: Preparation and Reactivity. *Tetrahedron* **56**, 9365-9373 (2000).

40. Neese, F. The ORCA program system. *Wiley Interdiscip. Rev.: Comput. Mol. Sci.* **2**, 73-78 (2012).

41. Schäfer, A., Horn, H. & Ahlrichs, R. Fully optimized contracted Gaussian basis sets for atoms Li to Kr. *J. Chem. Phys.* **97**, 2571-2577 (1992).

42. Gütlich, P.; Bill, E.; Trautwein, A. X., *Mössbauer Spectroscopy and Transition Metal Chemistry*. Springer Berlin Heidelberg: New York, 2011.

43. Römelt, M., Ye, S. & Neese, F. Calibration of Modern Density Functional Theory Methods for the Prediction of ^{57}Fe Mössbauer Isomer Shifts: Meta-GGA and Double-Hybrid Functionals. *Inorg. Chem.* 48, 784-785 (2009).